Power Electronic Systems
Laboratory

IEEE Transactions on Industrial Electronics, Vol. 58, No. 8, pp. 3264-3274, August 2011.

The Three-Phase Common-Mode Inductor: Modeling and Design Issues

M. L. Heldwein
L. Dalessandro
J. W. Kolar

Eidgenössische Technische Hochschule Zürich
Swiss Federal Institute of Technology Zurich

The Three-Phase Common-Mode Inductor: Modeling and Design Issues

Marcelo Lobo Heldwein, *Member, IEEE*, Luca Dalessandro, *Member, IEEE*, and Johann W. Kolar, *Fellow, IEEE*

***Abstract*—This paper presents a comprehensive physical characterization and modeling of the three-phase common-mode (CM) inductors along with the equivalent circuits that are relevant for their design. Modeling issues that are treated sparsely in previous literature are explained in this paper, and novel insightful aspects are presented. The calculation of the leakage inductance is reviewed, along with the magnetic core saturation issues, and a new expression for the leakage flux path is derived. The influence of the core material characteristics on the performance of the component is discussed, and a new method for the selection of the material for the minimized volume CM inductors is proposed in order to simplify the design procedure. Experimental results which validate the model are presented.**

***Index Terms*—Choke, common mode (CM), conducted emissions, EMC, inductor, three-phase systems.**

Index of Symbols

i	Current.
$\hat{I}$	Peak current.
i_X	Current at phase X.
$i_{\rm cm}$	Common-mode current.
$i_{\rm dm}$	Differential-mode current.
$i_{X,\rm dm}$	Differential-mode current at phase X.
$I_{L,\max}$	Maximum inductor current.
I_L	Inductor rms current.
u_X	Voltage at phase X.
$u_{\rm cm}$	Common-mode voltage.
$u_{X,\rm dm}$	Differential-mode voltage at phase X.
N_L	Number of turns per winding.
l_e	Average mean path length.
l_w	Wire length.
$d_{\rm wires}$	Insulation thickness between adjacent conductors.
ϕ_w	Wire diameter.
ρ_w	Wire resistivity.
μ_w	Wire permeability.
μ	Material permeability.
μ_o	Permeability of free space.
μ_r	Relative permeability.
$\vec{H}_{X,\rm leak}$	Magnetic field at phase X.
$\vec{H}_{\rm cm}$	Common-mode current generated field.
$H_{\rm int}$	Internal magnetic field.
$H_{\rm ext}$	External magnetic field.
$\vec{B}_{\rm cm}$	Common-mode current generated flux density.
$B_{\rm sat}$	Saturation flux density.
B	Flux density.
Φ	Magnetic flux.
L	Self-inductance of a winding.
M	Mutual inductance of the windings.
L_σ	Leakage inductance of a winding.
$L_{\rm air}$	Inductance of a core-less inductor.
$L_{\rm cm}$	Equivalent common-mode inductance.
$k_{\rm cm}$	Magnetic coupling coefficient.
A_L	Inductance per turn for a given core.
$\bar{\mu}$	Complex permeability.
μ'	Real component of the complex permeability.
μ''	Imaginary component of the complex permeability.
$R_{\rm CM,core}$	Core losses related common-mode resistance.
K_c, α, and β	Steinmetz loss coefficients.
$P_{\rm vol}$	Core losses per volume.
f	Frequency.
ω	Angular frequency.
$R_{\rm dc}$	Winding dc resistance.
$R_{\rm ac}$	Winding ac resistance.
$N_{\rm layers}$	Number of layers.
$l_{\rm eff}$	Effective mean path length.
θ	Winding angle.
ID	Inner diameter of a toroid.
OD	Outer diameter of a toroid.
$H_{\rm tor}$	Height of a toroid.
$Z_{\rm tor}$	Impedance of a wound toroid.
σ	Mechanical stress.
S	Cross section.
F	Load force.
ΔT	Temperature rise.
P_L	Inductor total losses.
S_L	Inductor surface area.
$R_{\rm th}$	Thermal resistance of an inductor.
$h_{\rm film}$	Film coefficient.
$K_{\rm th}$	Geometry coefficient.
Vol	Inductor volume.
A_e	Core effective area.
A_eA_w	Magnetic core product of areas.

Manuscript received June 23, 2010; revised September 8, 2010; accepted October 8, 2010. Date of publication October 28, 2010; date of current version July 13, 2011.

M. L. Heldwein is with the Electrical Engineering Department, Federal University of Santa Catarina (UFSC), 88040-970 Florianópolis, Brazil (e-mail: heldwein@inep.ufsc.br).

L. Dalessandro is with ALSTOM Power Thermal Products–Turbogenerators, 5242 Birr, Switzerland (e-mail: luca.dalessandro@power.alstom.com).

J. W. Kolar is with the Power Electronic Systems Laboratory, Swiss Federal Institute of Technology (ETH Zurich), 8092 Zurich, Switzerland (e-mail: kolar@lem.ee.ethz.ch).

Color versions of one or more of the figures in this paper are available online at http://ieeexplore.ieee.org.

Digital Object Identifier 10.1109/TIE.2010.2089949

I. Introduction

HIGH-POWER applications require a three-phase conversion of the electric energy. In particular, three-phase PWM converters have increased their market share due to clear advantages over other technologies. On the other hand, PWM converters present some side effects mainly due to the pulsed waveforms with rich spectral contents and very short transient times [1]. Thus, they typically require input filters to comply with the electromagnetic compatibility (EMC) requirements, and three-phase filters present a large demand from the industry. In this context, three-phase common-mode (CM) inductors find a large application [2] in areas such as adjustable-speed drives [3], [4], UPSs [5], renewable energy, process technology, battery charging for electric vehicles, power supplies for IT [6], future more electric aircrafts, and others.

In 1971, a three-phase version of the CM choke was presented [7], along with the main advantages of this type of construction in suppressing the CM propagated noise. Different methods can be applied to model a CM inductor, ranging from very simple analytical models to the characterization of the inductors based on the in-circuit measurements [8]. In this paper, the models that can be used to design a CM filter inductor are analyzed. The physics of a three-phase CM inductor is explained, and equivalent circuits are derived based on previous literature. The models take into account the core material characteristics and the geometrical configuration of the inductor. The calculation of the leakage inductance is reviewed, and a new model is introduced. Relevant magnetic core saturation issues and, in particular, the mechanisms of local magnetic core saturation are explained.

The use of a high switching frequency enables the reduction of the passive component volume, and it is the driving factor for the current increase [2], [9] in the power density of power converters. It is expected that this growth continues. Thus, the design of volume optimized components becomes very important. For the CM inductors, this motivates the research of accurate models and improved circuit topologies and the utilization of high-performance materials [10]. With this objective, a comparison among the available core materials is performed, with emphasis on material characteristics for filter application. Design issues such as leakage inductance and thermal models for wound toroidal inductors are analyzed, and a novel method for the selection of core materials is proposed for the design of the volume minimized CM inductors.

II. Three-Phase CM Inductor

The construction of a typical three-phase CM inductor for high-power applications is shown in Fig. 1. This arrangement has the advantages of employing toroidal cores: lower core costs, small leakage flux, and low thermal resistance (cf., Appendix A). The windings are physically arranged to withstand the electrical breakdown limits with respect to the line-to-line voltage across them. With this measure, it is possible to use a magnetic wire with standard coating, thus reducing the thermal resistance and costs compared to high-voltage insulated wires. The disadvantage is that the leakage flux arising from the differential-mode (DM) currents is higher than a tighter winding.

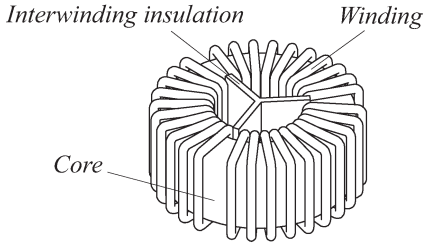

Fig. 1. Construction of a three-phase CM inductor.

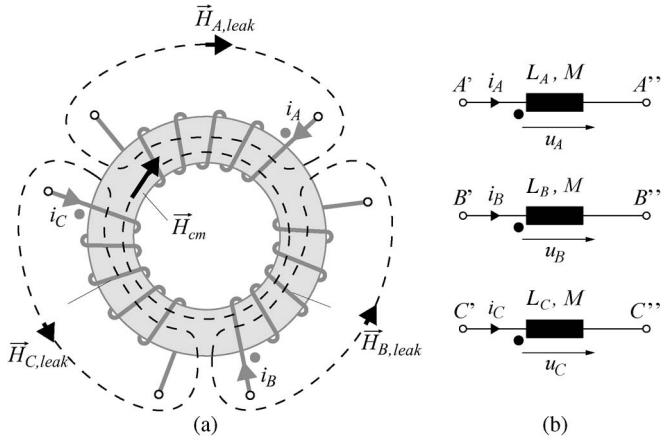

Fig. 2. (a) Currents and magnetic fields in a three-phase CM inductor with finite permeability. (b) Schematics of a purely inductive three-phase CM inductor.

Due to safety requirements, the maximum earth leakage currents are limited, and the value of the capacitors that can be connected from the ac power lines to the protective earth is limited to the nanofarad range. For a CM filter, this limitation implies, in the case of larger inductors, compensating for the small capacitors. If separated inductors are used at each power line, a large peak flux density is expected due to the large values of the low-frequency DM currents. Therefore, the low-permeability core materials would be required, leading to bulky inductors. There are three ways to reduce the magnetic field in a core, which are the following: 1) reduce the number of turns of the windings; 2) reduce the current; and 3) construct the windings in such a way that the fields created by each of them oppose the fields of the others so that the net field is reduced. The third alternative is explored in CM inductors by engineers since the early days of radio engineering [11], [12]. It was not until 1966 that this component received the name "common mode choke" [13] in the literature. In 1970, a mathematical model [12] was presented for a two-line inductor.

The principle of a conventional three-phase CM inductor is shown in Fig. 2(a). The CM current $i_{\rm cm}$ generates the magnetic fields in each of the windings, which are all on the same direction, and ideally, the total net field $(\vec{H}_{\rm cm})$ is the scalar sum of each single one. For DM currents $i_{A,\rm dm}$, $i_{B,\rm dm}$, and $i_{C,\rm dm}$, where

$$i_{A,\rm dm} + i_{B,\rm dm} + i_{C,\rm dm} = 0 \tag{1}$$

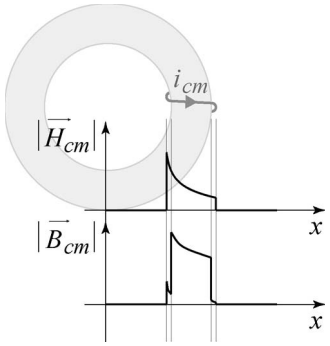

Fig. 3. Distributions of the magnetic field ($\vec{H}_{\rm cm}$) and flux density ($\vec{B}_{\rm cm}$) for the CM currents.

the net flux in the core for an infinite relative permeability and for the same number of turns N_L in the windings is

$$\frac{N_L i_{A,\rm dm}}{l_e} + \frac{N_L i_{B,\rm dm}}{l_e} + \frac{N_L i_{C,\rm dm}}{l_e} = 0. \tag{2}$$

Thus, an ideal three-phase CM inductor eliminates the influence of the DM currents. However, in case of a finite permeability, part of the magnetic field generated by the DM currents ($\vec{H}_{A,\rm leak}$, $\vec{H}_{B,\rm leak}$, and $\vec{H}_{C,\rm leak}$) is distributed through the surrounding media and is not negligible. This portion of the magnetic field is named *leakage field* and is responsible for a change in the internal fields, which must be considered. Thus, depending on the direction of the DM currents, the CM field is stronger or weaker in different portions of the core.

From the CM currents shown in Fig. 2(a), the magnetic field ($\vec{H}_{\rm cm}$) and the magnetic flux density ($\vec{B}_{\rm cm}$) present the distributions shown in Fig. 3, which are similar as that for the single-phase CM inductor [14]. An exponential distribution is expected, where the space that is close to the inner conductors presents a higher field than the external side.

The circuit schematics for a purely inductive and symmetrically built three-phase CM inductor are shown in Fig. 2(b). Three mutually coupled inductors reproduce the behavior previously explained from a circuit theory perspective. Considering that $L_A = L_B = L_C = L$, it follows that

$$\begin{bmatrix} u_A \\ u_B \\ u_C \end{bmatrix} = \begin{bmatrix} L & M & M \\ M & L & M \\ M & M & L \end{bmatrix} \cdot \frac{d}{dt} \begin{bmatrix} i_A \\ i_B \\ i_C \end{bmatrix}. \tag{3}$$

The mutual inductance M is defined by

$$M = k_{\rm cm} L. \tag{4}$$

From (3) and (4), two inductances can be evaluated. The CM inductance is due to three identical currents ($i_A = i_B = i_C = i_{\rm cm}$). Hence, $u_A = u_B = u_C = u_{\rm cm}$, and the resulting CM inductance $L_{\rm cm}$ is defined as

$$L_{\rm cm} = \frac{u_{\rm cm}}{di_{\rm cm}/dt} = L + M + M = L\frac{1 + 2k_{\rm cm}}{3} \tag{5}$$

where $k_{\rm cm}$ is the magnetic coupling coefficient among the different windings.

According to (5), the CM impedance is equivalent to the self-inductance of a winding if $k_{\rm cm} = 1$. This shows the importance of a high interwinding coupling in a CM inductor.

If three DM currents are considered, then $i_{A,\rm dm} + i_{B,\rm dm} + i_{C,\rm dm} = 0$, and $u_{A,\rm dm} + u_{B,\rm dm} + u_{C,\rm dm} = 0$. It follows that

$$\begin{bmatrix} u_{A,\rm dm} \\ u_{B,\rm dm} \\ u_{C,\rm dm} \end{bmatrix} = \begin{bmatrix} L-M & 0 & 0 \\ 0 & L-M & 0 \\ 0 & 0 & L-M \end{bmatrix} \cdot \frac{d}{dt} \begin{bmatrix} i_{A,\rm dm} \\ i_{B,\rm dm} \\ i_{C,\rm dm} \end{bmatrix}. \tag{6}$$

If the DM inductance is defined as the leakage inductance L_σ

$$L_\sigma = \frac{u_{i,\rm dm}}{di_{i,\rm dm}/dt} = L - M, \qquad \text{with} \quad i = A, B, C \tag{7}$$

it follows that

$$L_\sigma = L \cdot (1 - k_{\rm cm}). \tag{8}$$

If a coupling $k_{\rm cm} = 1$ is considered, the leakage inductance is zero. The effects of the DM inductances are not simple to model in a complete filter because of the external couplings with other components. The utilization of the DM inductances in filtering the DM currents might be very useful, but this application requires a careful analysis in order to reduce the radiated emissions and deterioration of the filtering performance due to external couplings.

From the previous analysis, the model of a CM inductor can be divided into two parts: one for the symmetrical currents and the other for the asymmetrical currents. This provides a useful simplification for the following analysis.

III. CM Inductor Design Parameters

A. CM Inductance

The three-phase CM inductor is made out of three windings in parallel and is wound in the same direction as the CM currents. Therefore, as for a conventional DM inductor, the self-inductance of the windings around the ferromagnetic core is dependent on the real part μ' of the complex permeability $\bar{\mu}$ [18]. However, unlike the DM inductors, the dependence of the permeability on the DM currents is typically very small due to the reduced net flux. Typical CM currents are of low amplitude so that the magnetic flux in the core does not create large variations in the core's permeability. Thus, the CM inductance $L_{\rm CM}$ can be defined as a function of the frequency f, number of turns N_L, and inductance per turn A_L of the core by

$$L_{\rm CM}(f) = A_L N_L^2 \cdot \frac{\mu'(f)}{|\bar{\mu}(f = 0\ \text{Hz})|}. \tag{9}$$

Since the CM currents typically generate low flux densities, high-permeability materials can be used to achieve small dimensions. The proper choice of core materials leads to compact inductors and reduced parasitics. Nevertheless, the materials for the CM inductors present a highly variable complex permeability with frequency. The real part of the series complex permeability for some high-performance magnetic materials is shown in Fig. 4(a). Two types of ferrite (N30 and T38 [16]), a

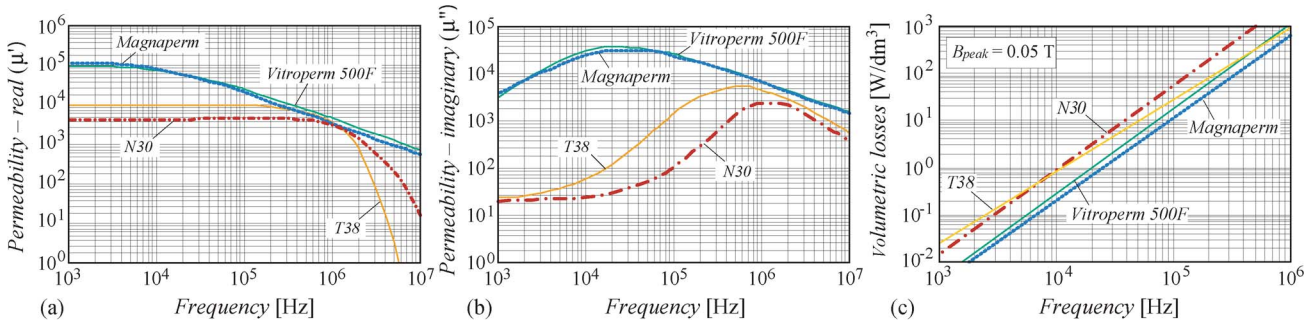

Fig. 4. Characteristics of the core materials for the CM inductors [15]–[17]. (a) Frequency-dependent magnitude of the real part of the relative complex permeability. (b) Magnitude of the imaginary part of the relative complex permeability. (c) Core losses as a function of the frequency for a peak flux density $B_{\text{peak}} = 0.05$ T.

nanocrystalline (VITROPERM 500F [15]), and an amorphous material (MAGNAPERM [17]) are compared. The real part of the permeability is similar in the 0.2–2 MHz range, but the nonferrite materials present higher permeabilities for other frequency ranges.

B. Losses and Associated Resistances

1) Resistance Due to Core Losses: The imaginary part μ'' of the complex permeability affects the small signal losses of the materials [18]. The increased losses cause the series impedance of the CM inductor to be increased with a resistive portion, which is significant for high frequency. Manufacturers provide curves [19] defining the imaginary part of the permeability as a function of the frequency $\omega = 2\pi f$, as shown in Fig. 4(b). The imaginary part is lower for ferrites. If the flux density can be treated as small signal, then the resistance can be calculated by

$$R_{\text{CM,core}} = A_L N_L^2 \omega \cdot \frac{\mu''}{|\bar{\mu}(f = 0\text{ Hz})|}. \tag{10}$$

Regarding the large signal losses, for the typical CM core materials, the eddy current losses are negligible [20]. The hysteresis and the residual losses can be modeled with the Steinmetz equation, relating the volumetric losses P_{vol} with the frequency f and flux density B

$$P_{\text{vol}} = K_c f^{\alpha} B^{\beta} \tag{11}$$

where K_c, α, and β are the characteristics of the materials, which are typically fitted for a frequency range. The losses data are shown in Fig. 4(c). Following [20], the series resistance that is due to large signal core losses can be modeled as

$$R_{\text{CM,core}} = 2V_c K_c f^{\alpha} I_L^{\beta-2} \left(\frac{A_L N_L \mu'(f)}{A_e \, |\bar{\mu}(f = 0\text{ Hz})|} \right)^{\beta}. \tag{12}$$

In order to compare the equivalent resistance, the material VITROPERM 500 F is chosen. Three resistances are calculated: one based on (10) and two based on (12), considering a current of 10 mA and 10 A. The resistances are shown in Fig. 5. The Steinmetz parameters are obtained from the regression of the data points from 10 to 300 kHz. Thus, the resistance for 10 mA approaches the one calculated with the permeability in this frequency range. This resistance increases for higher currents. For the design of the CM chokes, it is sufficient to calculate the resistance with the complex permeability, since higher currents lead to higher resistances and, thus, higher attenuation of the CM currents.

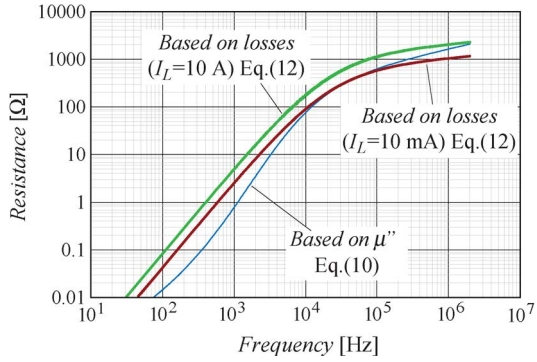

Fig. 5. Comparison of the series resistance that is due to core losses for material VITROPERM 500 F, core T6000-6-L2025-W380, and windings of seven turns.

The core losses are typically neglected when performing the thermal design of the CM chokes, unless a very high switching frequency is employed, or when installing inductors between three-phase inverters and motors, where very large CM voltages occur.

2) Series Winding Resistance: Considering a solid round conductor with length l_w and diameter ϕ_w and a material with relative permeability $\mu_w \cong 1$ and resistivity ρ_w, its dc resistance is

$$R_{w,\text{dc}} = \frac{4 l_w \rho_w}{\pi \phi_w^2}. \tag{13}$$

The inductors used in the power filters are typically designed on a single layer. This ensures that the winding parasitic capacitance is low and that the proximity effect can be neglected. Under this assumption, the resistance of the inductor's wire is dependent on the skin effect and on the conductor's characteristics. However, if a larger number of layers N_{layers} are required, the approach that is explained in [20] and that originated in [21] can be employed, leading to a resistance of

$$R_{w,\text{ac}} \cong R_{w,\text{dc}} \cdot A \cdot \left[1 + \frac{2\left(N_{\text{layers}}^2 - 1\right)}{3} \right] \tag{14}$$

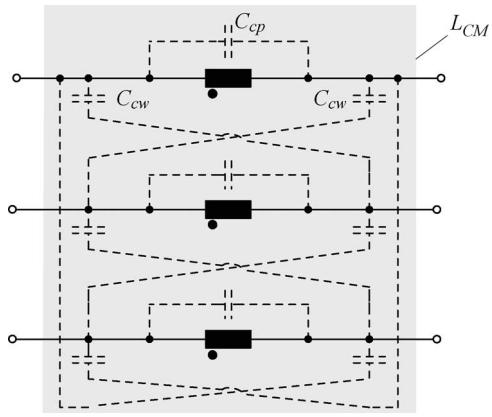

Fig. 6. Parasitic capacitance network model for a three-phase CM inductor.

with

$$A = \left(\frac{\pi}{4}\right)^{\frac{3}{4}} \cdot \frac{\sqrt{\phi_w^3}}{\delta\sqrt{d_{\text{wires}}}} \tag{15}$$

where d_{wires} indicates the distance between two adjacent conductors. In order to profit from the skin effect to achieve higher impedances at high frequency, solid round conductors are used instead of Litz wires [22]. The precise calculation of the winding losses has been analyzed in [23]–[27].

These expressions are valid for the frequency range f under the conditions

$$\text{if } N_{\text{layers}} = 1 \Rightarrow f \geq \frac{\rho_w d_{\text{wires}}}{\pi\mu_w\phi_w^3} \cdot \left(\frac{4}{\pi}\right)^{\frac{3}{2}} \tag{16}$$

$$\text{if } N_{\text{layers}} > 1 \Rightarrow f \geq \frac{16\rho_w d_{\text{wires}}}{\pi\mu_w\phi_w^3} \cdot \left(\frac{4}{\pi}\right)^{\frac{3}{2}}. \tag{17}$$

C. Parasitic Parallel Capacitance

For an inductor with the construction of Fig. 2(a), the most relevant parasitic capacitances are shown in Fig. 6, where the main contribution of the interwinding capacitances is due to the electrical field lines which start from a winding and terminate on other windings. The calculation of the winding parasitic parallel capacitances C_{cp} for a three-phase CM inductor can be done with the procedure presented in [28]–[30] for DM inductors. If the interwinding capacitance C_{cw} can be neglected, the resultant parallel capacitance for the CM currents is the parallel connection of the capacitances of the three windings. This is typically the case since the windings are separated by a distance which is much larger than the space among the turns of a winding.

D. Leakage Inductance and Its Saturation Issues

An assessment of the leakage inductance value for the single-phase CM inductors is done in [14]. This can be applied to the three-phase inductors. Assuming the symmetric magnetic fields shown in Fig. 2(a), each winding can be simplified to

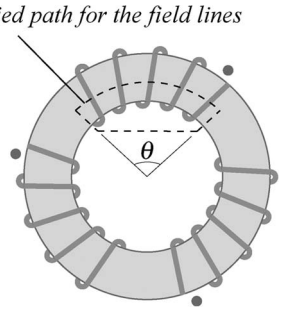

Fig. 7. Simplified magnetic field path for the leakage field.

an equivalent on a 120°-wide portion. The air coil inductance L_{air} is

$$L_{\text{air}} = \mu_o N_L^2 \frac{A_e}{l_{\text{eff}}} \tag{18}$$

where l_{eff} is the effective mean path length of the leakage magnetic field, which has two portions (inside and outside the core). The equation empirically derived in [14] gives

$$l_{\text{eff},N\text{ave}} = l_e\sqrt{\frac{\theta}{2\pi} + \frac{1}{\pi}\sin\frac{\theta}{2}} \tag{19}$$

which is valid for $\theta > \pi/6$ and which has l_e as the mean path length for the toroidal core.

The winding is modeled as wound on a rod, whose effective permeability is a function of the core permeability, rod length, and cross-sectional area A_e. This can be approximated by assuming high-permeability cores with a good accuracy [14], leading to a leakage inductance of

$$L_\sigma \cong 2.5\mu_o N_L^2 \frac{A_e}{l_{\text{eff}}}\left(\frac{l_e}{2}\sqrt{\frac{\pi}{A_e}}\right)^{1.45}. \tag{20}$$

The limit for the nonsaturation [14] of the core due to the DM current I_{dm} generated leakage flux is the saturation flux B_{sat}

$$\frac{L_\sigma I_{\text{dm}}}{N_L A_e} < B_{\text{sat}}. \tag{21}$$

According to (21), the calculation of the leakage flux density can be done with the estimated leakage inductance. Thus, saturation can already be avoided in the design phase. In [14], it is suggested that the value of the leakage inductance can be optimized for a given DM current so that the leakage inductance helps in filtering the DM emissions. In order to obtain a more detailed analysis of the saturation issues, finite element modeling is opportune [31].

E. New Empirical Expression for the Leakage Inductance Estimation

The simplified dashed path shown in Fig. 7 is used for the empirical formula of the effective mean path length

$$l_{\text{eff}} = \sqrt{\frac{OD^2}{\sqrt{2}}\left(\frac{\theta}{4}+1+\sin\frac{\theta}{2}\right)^2 + ID^2\left(\frac{\theta}{4}-1+\sin\frac{\theta}{2}\right)^2} \tag{22}$$

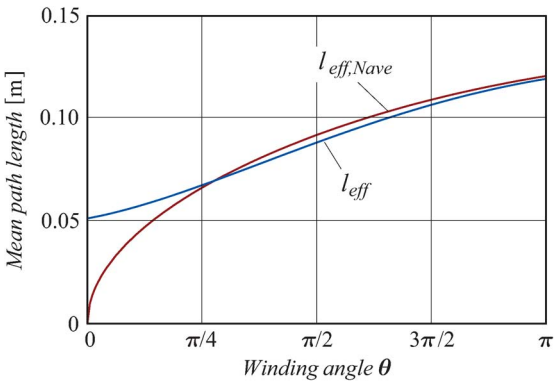

Fig. 8. Comparison of the results of (19) and (22) for a core with dimensions $OD = 50$ mm and $ID = 35$ mm.

where OD and ID are, respectively, the external and internal diameters and θ is the angle covered by each winding.

The comparison of (19) and (22) leads to Fig. 8 for a core of dimensions $OD = 50$ mm and $ID = 35$ mm. Both equations present close results for angles larger than $\pi/4$. This is also valid for cores with other dimensions.

F. Local and Global Magnetic Core Saturation

The CM inductor is desired to achieve an adequate inductance value in the presence of the CM noise currents. The magnetizing inductance value L is defined as

$$L = \frac{N_L B A_e}{i} \tag{23}$$

where B is the magnetic flux density, N_L is the number of turns, A_e is the area of the magnetic core cross section, and i represents the current. Once the magnetic core material is selected, the magnetic flux density saturation limit $B_{\rm sat}$ and the material permeability μ_r are given. Magnetic core saturation occurs as soon as the flux density in the core exceeds the saturation limit. Hence, the following condition should always be verified:

$$B = \frac{\Phi}{A_e} < B_{\rm sat}. \tag{24}$$

The number of turns N_L and the maximum current $\hat{I}$ are determined from (24) such that

$$\frac{N_L \hat{I}}{l_e} < \frac{B_{\rm sat}}{\mu_0 \mu_r}. \tag{25}$$

When magnetic core saturation occurs, the magnetic material no longer operates on the linear part of its characteristic (see Fig. 9), and the flux density rate in the core is zero. In this situation, the impedance of the device is equal to that of an air-cored device, and the impedance that is due to the core material is zero since it is directly proportional to the flux rate in it.

From (24) and (25), in order to avoid the core saturation, one has to do the following.

1) Reduce the net magnetic flux Φ in the core, or increase its cross-sectional area A_e.

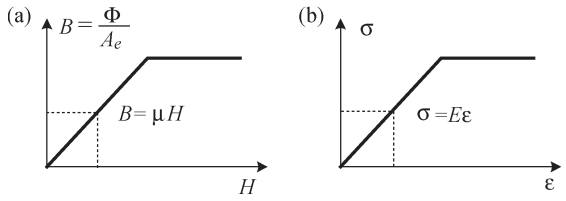

Fig. 9. One-value constitutive characteristic of the (a) magnetic and (b) elastic materials. The stress σ and the strain ε are proportional through the Young's modulus E after the Hooke's Law. The strength failure processes of the elastic materials are analogous to the saturation mechanisms of the magnetic materials.

2) Reduce the peak current $\hat{I}$.
3) Reduce the number of turns N.

The dimensioning of the CM inductor is a tradeoff between a small core size and an enough large core cross section to avoid saturation.

It should be noted that the effective cross-sectional area A_e of the core may decrease because of the local saturation of the magnetic material due to those pointwise values of the magnetic flux density which exceed the saturation limit (24). The local saturation may yield to the saturation of the whole cross section if the magnetic flux Φ remains constant. This saturation mechanism is analogous to the strength failure process which causes the cross section S of an elastic body to collapse. This process starts with a local failure of the cross section due to stresses σ that are larger than the critical stress σ_c that is admissible for the specific material

$$\sigma = \frac{F}{S} < \sigma_c. \tag{26}$$

The load F is then distributed over a smaller cross section. Hence, the value of the local stress σ increases. The cross section collapses as soon as the effective cross-sectional area S of the material is too small to fulfill the condition (26), which is a simple yield strength criterion. Two commonly used yield strength criteria are the Tresca's and Von Mises' criteria [32].

Knowledge of the strength failure processes, damage, and fracture [33] can be used to help explain the magnetic core saturation mechanisms, particularly the propagation of the local saturation over the cross section of a magnetic material.

Fig. 10 shows the examples of the local saturation of a magnetic material. The shaded regions shown in Fig. 10 represent the magnetic material saturated by an external magnetic field, as it may occur in the proximity of a turn wound around the core [see Fig. 10(a)], or by an internal field, whose field lines are typically gathered at the borders of the cross section for higher frequency [see Fig. 10(b)]. For each point of the cross section, the magnetic flux density is given by the effect of both the internal and external magnetic fields

$$B = \mu(H_{\rm int} + H_{\rm ext}). \tag{27}$$

Function (27) is the constitutive equation for the magnetic materials, and this form is valid under the assumption that the linearity and residual magnetization are equal to zero. The saturation limit for a magnetic material corresponds to the yield stress limit for an elastic material (see Fig. 9). According to (27), it is important that the net field within the core is small. A

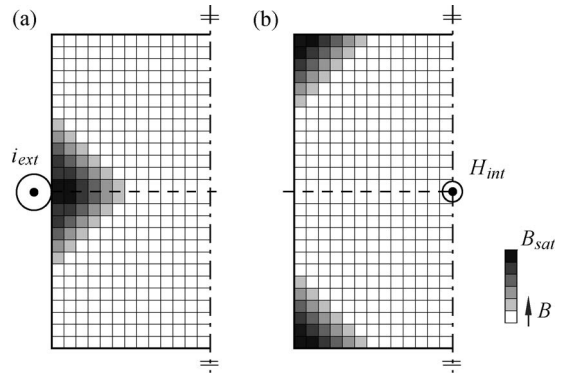

Fig. 10. Shaded regions represent the local saturation of the magnetic material (a) due to an external magnetic field and (b) due to the internal magnetic field distribution, respectively. Hence, the effective cross section of the magnetic material results is reduced.

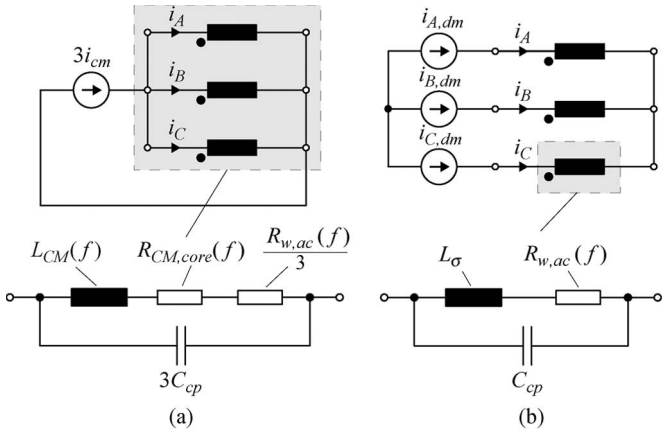

Fig. 11. Equivalent circuits for a three-phase CM inductor. (a) Equivalent circuits for CM. (b) Equivalent circuits for DM.

strategy that is used to reduce the magnetic field within the core is to construct the winding such that the fields created by each of them compensate the fields of the others.

IV. Three-Phase CM Inductor Equivalent Circuits

The three-phase CM inductor can be modeled with an equivalent circuit for CM and a different one for the DM currents. By doing this, the design of the CM and DM filters can be performed separately, and simpler models can be used [34].

For symmetrical winding arrangement and homogeneous core permeability, the impedances of the windings are balanced and in parallel for the CM currents. Thus, the circuit shown in Fig. 11(a) is valid for a wide frequency range. As the magnetic fields generated by the CM currents add up, a single inductor with the number of turns of a single winding models the self-impedance. The resistances of the windings are in parallel, as well as the parasitic capacitances of the windings C_{cp}.

The leakage flux is not appreciably affected by the permeability of the core because the flux lines are closed through the air. Thus, the leakage inductance is approximately constant with frequency and currents. The resistances that are due to the losses in the wires are frequency dependent but typically small for $f < 30$ MHz. As the leakage flux in the core is zero, the core losses can be neglected. The final equivalent circuit for the DM currents is shown in Fig. 11(b).

TABLE I
Specifications of the CM Inductors

Inductor	**CM-01**	**CM-02**
Core	T6000-6-L2025-W380	B64290-L567 (2 stacked)
Material	VITROPERM 500 F	N30
Manufacturer	VAC	EPCOS
Turns	10	8
Wire diameter	1.4 mm	1.5 mm
Core OD	25.0 mm	30.5 mm
Core ID	16.0 mm	20.0 mm
Core height	10.0 mm	12.5 mm (2×)

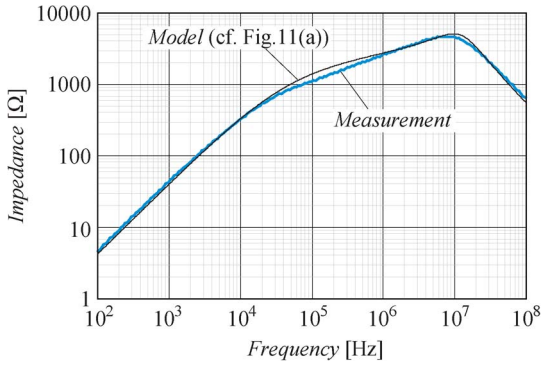

Fig. 12. CM impedance curves from the measurement and modeling of inductor **CM-01**.

Two three-phase CM inductors have been wound, for which the impedance measurements and the predicted models are compared in the following. The specifications of the inductors are given in Table I.

The CM impedance measurements were performed by connecting the three windings in parallel, as shown in Fig. 11(a). The impedances were measured by employing an Agilent 4294A Precision Impedance Analyzer that is capable of measuring the complex impedances from 40 Hz up to 110 MHz. The measured CM impedance of inductor **CM-01** is shown in Fig. 12 in comparison with the impedance calculated with the equivalent circuit of Fig. 11(a). A very good correlation among the curves is observed. The difference in the resonance frequency is due to the differences in the permeability curves with respect to the real one. The slight discrepancy from around 30–500 kHz is due to the differences between the actual permeability of the core and the values used in the calculations. This curve was fitted from the data sheet [15]. Considering the impedance curves up to approximately 20 kHz, the impedance increases at a rate of around +20 dB per decade, which means that the core losses can be neglected in this range and that the real part of the permeability is approximately constant. From 20 kHz to 6 MHz, the impedance increases at around +10 dB per decade due to the increasing imaginary part of the permeability. This increase also shows that the real part is not very important at this frequency range. At 8 MHz, the effect of the parallel capacitance starts to dominate the CM impedance, which starts to decrease at −20 dB per decade. Due to the high resistive part, the resonance peak is highly damped. This is a good characteristic since strong resonances might impair the

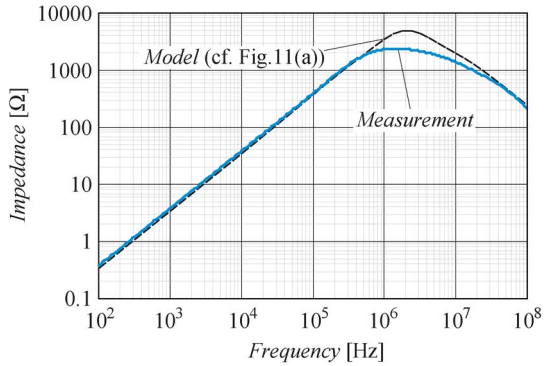

Fig. 13. CM impedance curves from the measurement and modeling of inductor **CM-02**.

TABLE II
LEAKAGE INDUCTANCES MEASURED AT 10 kHz

Inductor number	Calculated L_σ	Measured L_σ	Relative error
CM-01	1.85 μH	1.75 μH	5.7%
CM-02	4.89 μH	4.27 μH	14.5%

filtering performance. These curves show the importance of the correct modeling of the CM impedance of a CM inductor. If the complex permeability would be neglected, completely different curves would appear, misleading a filter design.

For the ferrite-based inductor (**CM-02**), the impedance curves are shown in Fig. 13, where the real part of the permeability dominates this design up to 1 MHz, and the influence of the losses is only observed at the resonance frequency. For this design, the permeability-curve-based model did not follow the impedance for a frequency higher than 1 MHz. The predicted parallel capacitance is close to the measured one since the impedance curves for very HF are in good agreement. The CM inductor built with ferrite has a more reactive characteristic when compared to the nanocrystalline-based one.

The leakage inductance of the three-phase CM inductors has been measured according to Appendix B using Agilent 4294A at 10 kHz (Table II). Errors smaller than 20% are observed, which are considered low in view of the involved simplifications. The larger inductor (**CM-02**) presents the largest inductance even with a lower number of turns. For the measurement of the leakage inductances, two windings have been shorted, while the impedance across the terminals of the third winding has been measured. This leads to an equivalent circuit where the leakage inductance of the measured winding is in series with the parallel connection of the other windings. The obtained experimental results validate the modeling procedure used in the design of the CM inductors and filters.

V. NOVEL APPROACH TO CORE MATERIAL SELECTION FOR CM INDUCTORS

The saturation flux densities for the used materials are $B_{\mathrm{sat,VITROPERM}} = 1.2$ T, $B_{\mathrm{sat,MAGNAPERM}} = 0.57$ T, and lower than 0.3 T for the ferrites. Regarding the maximum temperature for continuous operation, it is 120 °C for VITROPERM with a plastic enclosure (150 °C–180 °C for the core material itself under continuous operation), 90 °C for MAGNAPERM, and 100 °C for the ferrites. Comparing the characteristics of the materials shown in Fig. 4(a) and (b), VITROPERM 500 F presents the highest permeability. According to Fig. 4(c), the core losses for MAGNAPERM are the smallest, while they are higher for the ferrites.

TABLE III
RATIO $B_{\mathrm{sat}}/\sqrt{|\bar{\mu}|}$ FOR THE MATERIALS EMPLOYED IN THE CM INDUCTORS

Material	*Ratio* $\frac{B_{sat}}{\sqrt{\lvert\bar{\mu}\rvert}}$ @ 1 kHz	*Ratio* $\frac{B_{sat}}{\sqrt{\lvert\bar{\mu}\rvert}}$ @ 200 kHz
N30	3.7 mT	3.5 mT
T38	2.6 mT	2.7 mT
VITROPERM 500 F	3.8 mT	7.8 mT
MAGNAPERM	1.8 mT	3.9 mT

The choice of material aiming for the smallest volume core is a complex dependence on different parameters, like temperature, currents, impedance, and frequency of operation. Probably, the most important parameter is the saturation of the core. The following analysis proposes a method that is used to evaluate the material which leads to the smallest core dimensions.

The saturation of the core must be avoided for any current $\hat{I}$. Thus

$$N_L \hat{I} < \frac{l_e B_{\mathrm{sat}}}{\mu_o |\bar{\mu}|}. \tag{28}$$

The impedance Z_{tor} of a toroidal inductor with a core of height H_{tor} is

$$Z_{\mathrm{tor}} = \mu_o |\bar{\mu}| f N_L^2 H_{\mathrm{tor}} \cdot \ln\left(\frac{OD}{ID}\right) \tag{29}$$

from where the minimum number of turns for a given impedance and geometry is

$$N_L = \sqrt{\frac{1}{|\bar{\mu}|}} \underbrace{\sqrt{\frac{Z_{\mathrm{tor}}}{\mu_o f H_{\mathrm{tor}} \cdot \ln\left(\frac{OD}{ID}\right)}}}_{K_1}. \tag{30}$$

Replacing (30) in (28) leads to

$$\underbrace{\frac{K_1 I_{L,\max} \mu_o}{l_e}}_{K_2} < \frac{B_{\mathrm{sat}}}{\sqrt{|\bar{\mu}|}} \tag{31}$$

where K_2 is a constant if fixed frequency, geometry, current, and required impedance are assumed. With this result, the saturation condition for a CM inductor depends on the relation between two properties of the magnetic material, namely, its saturation flux density and the relative permeability. In Table III, this ratio is computed for the mentioned materials and is given for two different frequency values. The more favorable condition depends on the frequency range of interest. However, material VITROPERM 500 F shows the highest potential for both low and high frequencies.

VI. CONCLUSION

The three-phase CM toroidal inductors are thoroughly analyzed in this paper. A lumped-parameter equivalent circuit

is derived, and punctual references to previous literature are provided. The modeling aspects that are related to the physical construction of the toroidal three-phase CM inductors were addressed, and a novel method for the selection of the core materials was proposed for the volume minimization of the CM inductors.

The impedances of the model present a strong dependence on the construction and the core material. A method for the selection of the material for the CM inductors was proposed, which simplifies the design and allows for the minimum volume inductors in a given frequency range of application. The calculation of the leakage inductance was reviewed, along with the related saturation issues, and a novel expression was proposed. The experimental results validate the modeling procedure.

Furthermore, the mechanisms of the capacitive noise coupling in the three-phase EMC filters were briefly described. The main parasitic capacitive connections are constituted by the parasitic capacitances of the used filtering inductors. These effects can be reduced by using the capacitance cancellation techniques.

Appendix A
Thermal Models for the Toroidal Cores

The temperature rise of a filter inductor typically defines a core for a given application due to the employed material temperature limitations. Aiming for the smallest size, consequently cheaper cores, forces a filter designer to search for the most precise thermal models. Core manufacturers such as Magnetics Inc. [35] and Micrometals Inc. [36] and specialized literature [37] suggest that the expression

$$\Delta T = \left(\frac{P_L \ [\mathrm{mW}]}{S_L \ [\mathrm{cm}^2]} \right)^{0.833} \tag{32}$$

where P_L is the total inductor losses and S_L is the wound inductor surface are, provides a good approximation of the temperature rise ΔT in a core. This is a difficult calculation since the exact computation of the outer surface of an inductor might prove to be a big challenge. The assumption for this expression is that the inductor presents a 40% filling factor, and it is typically mounted on a printed circuit board. Thus, this is a special case of heat transfer based on typical boundary conditions. The classical expression for the convection-based thermal resistance R_{th} of a body of surface S_L is given by

$$R_{\mathrm{th}} = \frac{1}{h_{\mathrm{film}} S_L} \tag{33}$$

where the film coefficient h_{film} is strongly dependent on the boundary conditions, i.e., in parameters like material characteristics, temperature, surrounding media, surface finish, distance to other bodies, and air or fluid speed. The film coefficient can easily vary by orders of magnitude depending on air speed and distance to other bodies. A more easily applicable model based on (33) is proposed in [38], where the thermal resistance R_{th} of a core is calculated with

$$R_{\mathrm{th}} = \frac{\Delta T}{P_L} = \frac{K_{\mathrm{th}}}{Vol^{2/3}} \tag{34}$$

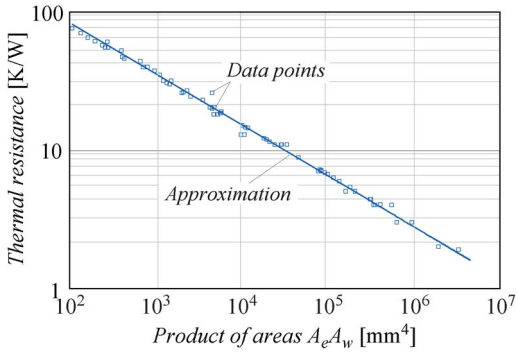

Fig. 14. Thermal resistance of the toroidal cores from different manufacturers [15], [35], [36] as presented in their catalogs and proposed approximation.

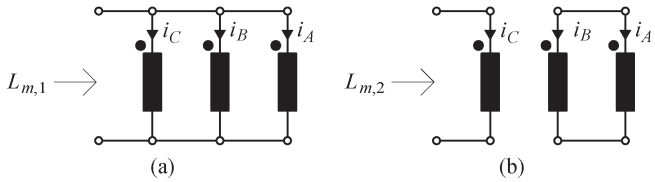

Fig. 15. Inductance measurements performed in order to evaluate the leakage inductance of a three-phase CM inductor.

where, instead of the outer surface, the volume Vol of the inductor is used and a coefficient K_{th} depends on the geometry of the core and on the film coefficient for convection. Coefficient K_{th} is fairly constant for a given core family if the dimensions of the cores are proportional and the same type of convection (natural or forced air) is applied. This coefficient can be calculated with the expression

$$K_{\mathrm{th}} = \frac{Vol^{2/3}}{h_{\mathrm{film}} S_L} \tag{35}$$

where h_{film} is the film coefficient for the given material and convection, which typically varies from 10 to 25 W/m^2 for natural convection [38]. This method [38] shows that it is possible to relate the thermal resistance of an inductor to its volume. However, during the design phase of an inductor, the product of the areas $A_e A_w$ is sometimes a more useful parameter than the volume, and a relation between the product of the areas and volume does exist. Therefore, it should be possible to define the thermal resistance of an inductor by its product of the areas.

In order to have a practical approach to define the thermal resistance, different toroidal core manufacturers [15], [35], [36], which provide the measured thermal resistances of their cores, have been researched. The result is shown in the graph of Fig. 14, where the thermal resistance of the cores from different manufacturers is plotted against the core product of the areas. An exponential tendency in the data points can be observed, which can be approximated by least squares regression to

$$R_{\mathrm{th}} \cong 415.17 \left(A_e A_w \ [\mathrm{mm}^4] \right)^{-0.3593} \ [\mathrm{K/W}] \tag{36}$$

leading to an R-squared factor of $R^2 = 0.9979$. The model obtained with (36) is only valid for the toroidal cores that are typically mounted in printed circuit boards, having the advantage of being a good approximation for the measured thermal resistance of many different cores and core manufacturers.

APPENDIX B
LEAKAGE INDUCTANCE MEASUREMENT

Different measurements can be used to estimate the leakage inductance of a CM inductor. Here, the measurements shown in Fig. 15 are performed. Based on the measured values of $L_{m,1}$ and $L_{m,2}$, the leakage inductance expression is derived in the following.

From the circuits in Fig. 15 and considering (3), it follows that

$$L_{m,1} = \frac{L}{3} + \frac{2M}{3} \tag{37}$$

$$L_{m,2} = \frac{L^2 + L\,M - 2M^2}{L + M}. \tag{38}$$

Solving the system gives the values of L and M. Replacing these values into (7) leads to

$$L_\sigma = \frac{6L_{m,1}\,L_{m,2}}{9L_{m,1} - L_{m,2}}. \tag{39}$$

REFERENCES

[1] E. Zhong and T. A. Lipo, "Improvements in EMC performance of inverter-fed motor drives," *IEEE Trans. Ind. Appl.*, vol. 31, no. 6, pp. 1247–1256, Nov./Dec. 1995.

[2] M. L. Heldwein and J. W. Kolar, "Impact of EMC filters on the power density of modern three-phase PWM converters," *IEEE Trans. Power Electron.*, vol. 24, no. 6, pp. 1577–1588, Jun. 2009.

[3] M. C. Di Piazza, G. Tine, and G. Vitale, "An improved active common-mode voltage compensation device for induction motor drives," *IEEE Trans. Ind. Electron.*, vol. 55, no. 4, pp. 1823–1834, Apr. 2008.

[4] A. F. Moreira, P. M. Santos, T. A. Lipo, and G. Venkataramanan, "Filter networks for long cable drives and their influence on motor voltage distribution and common-mode currents," *IEEE Trans. Ind. Electron.*, vol. 52, no. 2, pp. 515–522, Apr. 2005.

[5] L. Palma, M. H. Todorovic, and P. N. Enjeti, "Analysis of common-mode voltage in utility-interactive fuel cell power conditioners," *IEEE Trans. Ind. Electron.*, vol. 56, no. 1, pp. 20–27, Jan. 2009.

[6] T. Nussbaumer, M. L. Heldwein, and J. W. Kolar, "Differential mode input filter design for a three-phase buck-type PWM rectifier based on modeling of the EMC test receiver," *IEEE Trans. Ind. Electron.*, vol. 53, no. 5, pp. 1649–1661, Oct. 2006.

[7] D. R. Bush, "The common-core filter as an electromagnetic interference-suppression device," *IBM J. Res. Develop.*, vol. 15, no. 3, pp. 242–244, May 1971.

[8] J. Deng and K. Y. See, "In-circuit characterization of common-mode chokes," *IEEE Trans. Electromagn. Compat.*, vol. 49, no. 2, pp. 451–454, May 2007.

[9] H. Ohashi, "Possibility of power electronics paradigm shift with wide band gap semiconductors," *Mater. Sci. Forum*, vol. 457–460, pt. 1, pp. 21–26, 2004.

[10] M. L. Heldwein, H. Ertl, J. Biela, and J. W. Kolar, "Implementation of a transformerless common-mode active filter for offline converter systems," *IEEE Trans. Ind. Electron.*, vol. 57, no. 5, pp. 1772–1786, May 2010.

[11] F. E. King, "Baluns as EMC control devices," in *Proc. IEEE Int. Symp. Electromagn. Compat.*, 1970, pp. 53–60.

[12] T. H. Herring, "The common mode choke," in *Proc. IEEE Int. Symp. Electromagn. Compat.*, 1970, pp. 45–52.

[13] R. D. Rothenberger, C. Rapids, and J. Krauser, "Common mode choke for plural groups of memory array drive-return line pairs," U.S. Patent 3 482 227, Dec. 2, 1969.

[14] M. J. Nave, "On modeling the common mode inductor," in *Proc. IEEE Int. Symp. Electromagn. Compat.*, 1991, pp. 452–457.

[15] *Nanocrystalline Vitroperm EMC Components*, Vacuumschmelze (VAC) GmbH Co., Hanau, Germany, 2004.

[16] *Ferrites and Accessories—Materials*, EPCOS AG, Munich, Germany, 2006.

[17] *MAGNAPERM—High Permeability Toroidal Cores*, Metglas, Inc., Conway, SC, 2003.

[18] Q. Yu, T. W. Holmes, and K. Naishadham, "RF equivalent circuit modeling of ferrite-core inductors and characterization of core materials," *IEEE Trans. Electromagn. Compat.*, vol. 44, no. 1, pp. 258–262, Feb. 2002.

[19] S. Jing and Q. Jiang, "An alternative method to determine the initial permeability of ferrite core using network analyzer," *IEEE Trans. Electromagn. Compat.*, vol. 47, no. 3, pp. 651–657, Aug. 2005.

[20] M. Bartoli, A. Reatti, and M. K. Kazimierczuk, "Modelling iron-powder inductors at high frequencies," in *Conf. Rec. IEEE IAS Annu. Meeting*, 1994, vol. 2, pp. 1225–1232.

[21] P. L. Dowell, "Effects of eddy currents in transformer windings," *Proc. Inst. Elect. Eng.*, vol. 113, no. 8, pp. 1387–1394, Aug. 1966.

[22] K. de Jager, L. Dalessandro, I. W. Hofsajer, and W. G. Odendaal, "Wave analysis of multilayer absorptive low-pass interconnects," in *Proc. IEEE Power Electron. Spec. Conf.*, 2007, pp. 2121–2127.

[23] M. K. Kazimierczuk, *High-Frequency Magnetic Components*. New York: Wiley, 2009.

[24] D. Murthy-Bellur and M. K. Kazimierczuk, "Harmonic winding loss in buck dc–dc converter for discontinuous conduction mode," *IET Power Electron.*, vol. 3, no. 5, pp. 740–754, Sep. 2010.

[25] N. Kondrath and M. K. Kazimierczuk, "Inductor winding loss owing to skin and proximity effects including harmonics in non-isolated pulse-width modulated dc–dc converters operating in continuous conduction mode," *IET Power Electron.*, vol. 3, no. 6, pp. 989–1000, Nov. 2010.

[26] H. Sekiya and M. K. Kazimierczuk, "Design of RF-choke inductors using core geometry coefficient," in *Proc. Elect. Manuf. Coil Winding Conf.*, Nashville, TN, 2009, p. 10.

[27] M. K. Kazimierczuk and H. Sekiya, "Design of ac resonant inductors using area product method," in *Proc. IEEE ECCE*, 2009, pp. 994–1001.

[28] A. Massarini and M. K. Kazimierczuk, "Self-capacitance of inductors," *IEEE Trans. Power Electron.*, vol. 12, no. 4, pp. 671–676, Jul. 1997.

[29] G. Grandi, M. K. Kazimierczuk, A. Massarini, and U. Reggiani, "Stray capacitances of single-layer solenoid air-core inductors," *IEEE Trans. Ind. Appl.*, vol. 35, no. 5, pp. 1162–1168, Sep./Oct. 1999.

[30] L. Dalessandro, F. da Silveira Cavalcante, and J. W. Kolar, "Self-capacitance of high-voltage transformers," *IEEE Trans. Power Electron.*, vol. 22, no. 5, pp. 2081–2092, Sep. 2007.

[31] H. Chen, Z. Qian, S. Yang, and C. Wolf, "Finite-element modeling of saturation effect excited by differential-mode current in a common-mode choke," *IEEE Trans. Power Electron.*, vol. 24, no. 3, pp. 873–877, Mar. 2009.

[32] A. Carpinteri, *Structural Mechanics—A Unified Approach*. Oxford, NY: Chapman & Hall, 1997.

[33] C. A. Brebbia and A. Carpinteri, *Damage and Fracture Mechanics*. Boston, MA: Comput. Mech. Publ., 1998.

[34] L. Dehong and J. Xanguo, "High frequency model of common mode inductor for EMI analysis based on measurements," in *Proc. IEEE Int. Symp. Electromagn. Compat.*, 2002, pp. 462–465.

[35] *Powder Cores—Molypermalloy, High Flux, Kool mu—2005/2006 Catalog*, Magnetics, Inc., Pittsburgh, PA, 2005.

[36] *Micrometals Catalog CD-ROM*, Micrometals Inc., Anaheim, CA, 2005.

[37] M. Bartoli, A. Reatti, and M. K. Kazimierczuk, "Minimum copper and core losses power inductor design," in *Conf. Rec. IEEE IAS Annu. Meeting*, 1996, vol. 3, pp. 1369–1376.

[38] L. M. Escribano, P. Zumel, R. Prieto, J. A. Oliver, and J. A. Cobos, "A very simple analytical approach of thermal modeling for magnetic components," in *Proc. IEEE Appl. Power Electron. Conf. Expo.*, 2005, vol. 3, pp. 1944–1950.

Marcelo Lobo Heldwein (S'99–M'08) received the B.S. and M.S. degrees in electrical engineering from the Federal University of Santa Catarina (UFSC), Florianópolis, Brazil, in 1997 and 1999, respectively, and the Ph.D. degree from the Swiss Federal Institute of Technology (ETH Zurich), Zurich, Switzerland, in 2007.

From 1999 to 2001, he was a Research Assistant with the Power Electronics Institute (INEP), UFSC. From 2001 to 2003, he was an Electrical Design Engineer with Emerson Energy Systems, So Jos dos Campos, Brazil, and Stockholm, Sweden. He was a Postdoctoral Fellow with the Power Electronics Institute (INEP), UFSC, under the PRODOC/CAPES program from 2008 to 2009. He is currently an Adjunct Professor with the Electrical Engineering Department, UFSC. His research interests include power factor correction techniques, static power conversion, and electromagnetic compatibility.

Dr. Heldwein is a member of the Brazilian Power Electronic Society (SOBRAEP).

Luca Dalessandro (S'02–M'07) received the M.Sc. degree (first class honors) in electrical engineering from the Politecnico di Bari, Bari, Italy, in 2001 and the Ph.D. degree in electrical engineering from the Swiss Federal Institute of Technology (ETH Zurich), Zurich, Switzerland, in 2007.

From 2001 to 2002, he was a Researcher with the Max-Planck Institute for Mathematics in the Sciences (MPI-MIS), Leipzig, Germany. From 2002 to 2006, he was a Research and Teaching Assistant with the Power Electronics Systems Laboratory (PES), ETH Zurich. In the summer of 2006, under a postdoctoral fellowship grant provided by the industry, he joined the National Science Foundation Engineering Research Center (NSF-ERC) for Power Electronics Systems (CPES), Virginia Polytechnic Institute and State University (Virginia Tech), Blacksburg. In the fall of 2006, he was appointed as an Adjunct Professor with the Bradley Department of Electrical and Computer Engineering, Virginia Tech. From 2007 to 2010, he was a Guest Research Associate with the Power Systems and High-Voltage Technology Institute (EEH), ETH Zurich. In 2007, he initiated an ETH spin-off company in the field of high-performance current sensing. Since 2008, he has been with the R&D Department, ALSTOM Power, Birr, Switzerland, covering several functions as a Project Manager, Product Line Manager, and Patent Officer in the field of large synchronous machines, power generation, and power conversion. He has been an Invited Lecturer, Visitor, and Consultant for several recognized institutions and companies, including the Massachusetts Institute of Technology, Cambridge; the National Japanese Institute for Advanced Industrial Science and Technology (AIST), Japan; the Swiss Embassy in Italy; and Asea Brown Boveri (ABB). He has authored more than 30 peer-reviewed technical papers and patents. His research interests include all disciplines of electrical power engineering.

Dr. Dalessandro is a recipient of several awards and fellowships.

Johann W. Kolar (M'89–SM'04–F'10) received the M.Sc. and Ph.D. degrees (*summa cum laude*/promotio sub auspiciis praesidentis rei publicae) from the University of Technology Vienna, Vienna, Austria.

Since 1984, he has been working as an independent international consultant who is in close collaboration with the University of Technology Vienna, in the fields of power electronics, industrial electronics, and high-performance drives. He has proposed numerous novel PWM converter topologies and modulation and control concepts, e.g., the VIENNA rectifier and the three-phase ac–ac sparse matrix converter. He was appointed as a Professor and the Head of the Power Electronic Systems Laboratory, Swiss Federal Institute of Technology (ETH Zurich), Zurich, Switzerland, on February 1, 2001. He initiated and/or is the founder/cofounder of four spin-off companies targeting ultrahigh speed drives, multidomain/level simulation, ultracompact/efficient converter systems, and pulsed power/electronic energy processing. He has published over 350 scientific papers in international journals and conference proceedings and has filed 75 patents. The focus of his current research is on ac–ac and ac–dc converter topologies with low effects on the mains, e.g., for the power supply of data centers, more electric aircraft, and distributed renewable energy systems. Further main areas of research are the realization of ultracompact and ultraefficient converter modules employing the latest power semiconductor technology (e.g., SiC), novel concepts for cooling and EMI filtering, multidomain/scale modeling/simulation and multiobjective optimization, physical-model-based lifetime prediction, pulsed power, and ultrahigh speed and bearingless motors.

Dr. Kolar received the Best Transactions Paper Award from the IEEE Industrial Electronics Society in 2005, the Best Paper Award of the International Conference on Power Electronics in 2007, the 1st Prize Paper Award of the IEEE IAS IPCC in 2008, the IEEE IECON Best Paper Award of the IES PETC in 2009, the 2009 IEEE Power Electronics Society Transaction Prize Paper Award, and the 2010 Best Paper Award of the IEEE/ASME TRANSACTIONS ON MECHATRONICS. He also received an Erskine Fellowship from the University of Canterbury, Christchurch, New Zealand, in 2003. He is a member of The Institute of Electrical Engineers of Japan and the international steering committees and technical program committees of numerous international conferences in the field (e.g., Director of the Power Quality Branch of the International Conference on Power Conversion and Intelligent Motion). He is the Founding Chairman of the IEEE PELS Austria and Switzerland Chapter and the Chairman of the Education Chapter of the EPE Association. From 1997 to 2000, he was an Associate Editor of the IEEE TRANSACTIONS ON INDUSTRIAL ELECTRONICS, and since 2001, he has been an Associate Editor of the IEEE TRANSACTIONS ON POWER ELECTRONICS. Since 2002, he has also been an Associate Editor of the *Journal of Power Electronics* of the Korean Institute of Power Electronics and a member of the Editorial Advisory Board of the *IEEJ Transactions on Electrical and Electronic Engineering*.